JGR Atmospheres

RESEARCH ARTICLE
10.1029/2021JD036387

This article is a companion to She et al. (2021), https://doi.org/10.1029/2021JD036291.

Key Points:

- Seasonal variations of gravity wave-induced thermal (K_H) and constituent (K_{Wave}) diffusivities are deduced from lidar temperature data
- Wave-induced heat and constituent diffusivities in the mesopause at Ft. Collins exhibit strong annual oscillations with maxima in winter
- K_H and K_{Wave} are comparable to measurements made at other mid-latitude mountain sites in both hemispheres, including the seasonality

Supporting Information:

Supporting Information may be found in the online version of this article.

Correspondence to:

C. S. Gardner,
cgardner@illinois.edu

Citation:

Gardner, C. S., She, C.-Y., & Yan, Z.-A. (2022). Seasonal variations of gravity wave induced thermal and constituent diffusivities in the mesopause region above Ft. Collins, CO (40.6°N, 105.1°W). *Journal of Geophysical Research: Atmospheres*, *127*, e2021JD036387. https://doi.org/10.1029/2021JD036387

Received 20 DEC 2021
Accepted 9 MAR 2022

Author Contributions:

Conceptualization: Chester S. Gardner
Data curation: Zhao-Ai Yan
Formal analysis: Chester S. Gardner
Funding acquisition: Chester S. Gardner
Investigation: Chiao-Yao She
Methodology: Chester S. Gardner
Software: Chiao-Yao She, Zhao-Ai Yan
Supervision: Chester S. Gardner
Validation: Chiao-Yao She, Zhao-Ai Yan

Seasonal Variations of Gravity Wave Induced Thermal and Constituent Diffusivities in the Mesopause Region Above Ft. Collins, CO (40.6°N, 105.1°W)

Chester S. Gardner[1], Chiao-Yao She[2], and Zhao-Ai Yan[3,4]

[1]Department of Electrical & Computer Engineering, University of Illinois, Urbana, IL, USA, [2]Department of Physics, Colorado State University, Ft. Collins, CO, USA, [3]National Space Science Center, Chinese Academy of Sciences, Beijing, China, [4]University of Chinese Academy of Sciences, Beijing, China

Abstract Quasi-random vertical displacement fluctuations, caused by the spectrum of non-breaking gravity waves, mix the atmosphere, similar to turbulence, which induces significant vertical transport of heat and constituents in the upper atmosphere. Multi-decade observations of temperature, made between 85 and 100 km with a Na lidar at Colorado State University (CSU, 40.6°N, 105.1°W), are used to derive the seasonal variations of the wave-induced thermal (K_H) and constituent (K_{Wave}) diffusivities. Both show strong annual oscillations with maxima in winter, which increase with increasing altitude. K_H and K_{Wave} exhibit summer minima of ∼40 and ∼70 m^2s^{-1}, respectively, that are approximately constant with altitude. In winter, K_H varies from ∼50 at 85 to ∼180 m^2s^{-1} at 100 km, while K_{Wave} varies from ∼110 at 85 to ∼340 m^2s^{-1} at 100 km. These values are much larger than the eddy diffusivity (K_{zz} ∼ 35 m^2s^{-1}) predicted for this site by the Whole Atmosphere Community Climate Model. The CSU diffusivities are comparable to similar measurements made at other mid-latitude mountain sites in both hemispheres, and derived from global observations of atomic O. However, the seasonal variations differ from the O observations, which may reflect differences in wave sources at these sites and the different approaches employed to derive the wave diffusivities. Even so, the CSU results demonstrate that heat and constituent transport by unresolved, non-breaking gravity waves are important processes that need to be incorporated in global chemistry models to properly characterize the thermal and constituent structure of the upper atmosphere.

1. Introduction

Gravity waves in the mesosphere and lower thermosphere (MLT) play an important role in the vertical transport of both heat and constituents. Breaking gravity waves generate turbulence, which induces the diffusive transport of both heat and constituents via eddy mixing. Non-breaking gravity waves also drive strong vertical mixing of the atmosphere, which produces net heat and constituent fluxes (Gardner & Yang, 1998; Hickey et al., 2000; Liu, 2021; Liu & Gardner, 2004, 2005; Walterscheid, 1981; Weinstock, 1983), enhances molecular and eddy diffusion by perturbing constituent mixing ratios (Gardner, 2018; Grygalashvyly et al., 2012), and induces the chemical transport of reactive species by perturbing chemical reactions (Gardner & Liu, 2016; Walterscheid & Schubert, 1989). It has been known for decades that vertical transport induced by propagating gravity waves can be substantial. Walterscheid and Schubert (1989) used a dynamical-chemical model to show that the combined effects of wave dynamics and perturbed chemistry associated with the passage of a gravity wave can result in large downward fluxes of O_3 and OH near 80 km, which alters the mixing ratios of these species and their eddy and molecular diffusion. Hickey et al. (2000) used a 2-D nonlinear model to demonstrate that gravity waves can significantly alter the time averaged atomic O profile in the MLT through the constituent fluxes that the waves induce. Liu and Gardner (2004 and 2005) and Gardner and Liu (2010) directly measured the vertical Na flux profiles induced by gravity waves in the MLT at the Starfire Optical Range (SOR), NM (35°N) and atop Haleakalā volcano in Maui, HI (21°N). Those observations also showed that wave transport of Na was significant and generally much larger than transport by eddy and molecular diffusion.

Despite this early work, few if any of the global atmospheric chemical models incorporate wave-induced transport because they cannot resolve the important smaller-scale waves. However, this situation is now changing. Grygalashvyly et al. (2012) employed an effective wave diffusivity (K_{Wave}), equivalent to enhancing the eddy and molecular diffusivities, in a numerical model to study the impact of gravity waves on the transport of minor

Writing – original draft: Chester S. Gardner
Writing – review & editing: Chester S. Gardner, Chiao-Yao She

constituents in the MLT. Gardner and Liu (2016) derived generalized theoretical expressions for the chemical fluxes of neutral species induced by waves and turbulence and explored the impact on the transport of O_3, Na, and Fe in the MLT. Gardner et al. (2019) showed how the effective wave-driven constituent and thermal diffusivities ($K_{\rm Wave}$ and $K_{\rm H}$) can be derived from the gravity wave parameterizations incorporated in many global models. Most recently, Liu (2021) employed the concept of scale invariance to extrapolate the thermal diffusivity ($K_{\rm H}$) arising from the large-scale waves resolved by global models, to include the contributions from the unresolved small-scale waves.

In this paper, we use the multi-decade observations of the mesopause region temperature structure made by a Na Doppler lidar at Ft. Collins, CO (40.6°N, 105.1°W) to characterize the seasonal variations of the gravity wave-induced transport of heat and constituents as quantified by $K_{\rm H}$ and $K_{\rm Wave}$. This extensive data set is unique, consisting of Na lidar observations of the mesopause region temperature profile collected at relatively high vertical and temporal resolutions during the 20-year period from March 1990 to 2010 (She et al., 2022). The data set includes 956 nights of observations that are roughly evenly distributed over the spring, summer, autumn, and winter seasons, which enables us to accurately characterize the seasonal variations of wave activity and heat and constituent transport at this mid-latitude site.

2. Theoretical Background

The theoretical expression for the vertical constituent flux of a chemically active species, induced by non-breaking gravity waves is given by Equations 1–4 in Gardner et al. (2019) by simply setting the eddy and molecular diffusivities to zero and multiplying the transport velocities by the species density.

$$\overline{\mathrm{w}'\rho_{\mathrm{C}}'} = \overline{\rho}_{\mathrm{C}}\frac{\overline{\mathrm{w}'\rho_{\mathrm{A}}'}}{\overline{\rho}_{\mathrm{A}}} - \overline{\rho}_{\mathrm{C}}\left(\frac{\mathrm{g}}{\mathrm{R}\overline{\mathrm{T}}} + \frac{1}{\overline{\mathrm{T}}}\frac{\partial\overline{\mathrm{T}}}{\partial \mathrm{z}} + \frac{1}{\overline{\rho}_{\mathrm{C}}}\frac{\partial\overline{\rho}_{\mathrm{C}}}{\partial \mathrm{z}}\right)\mathrm{K}_{\mathrm{Wave}} + \overline{\mathrm{w}'\rho_{\mathrm{C}}'}_{\mathrm{Chemical}} \tag{1}$$

The prime denotes the wave driven perturbations and the overbar denotes the mean quantity. The parameters ρ_A and ρ_C are the atmospheric and constituent number densities, T is the temperature, w is the vertical velocity, $g = 9.5\ \mathrm{ms}^{-2}$ is the gravitational acceleration, $R = 287\ \mathrm{m}^2\mathrm{K}^{-1}\mathrm{s}^{-2}$ is the gas constant for dry air, and $K_{\rm Wave}$ is the effective wave-induced constituent diffusivity. The first term on the right-hand-side of the (1) is the contribution from the vertical Stokes drift ($\overline{\mathrm{w}'\rho_{\mathrm{A}}'}/\overline{\rho}_{\mathrm{A}}$) imparted to the atmosphere by the spectrum of gravity waves (e.g., Coy et al., 1986; Walterscheid & Hocking, 1991). The second term is the classical diffusive flux (e.g., Colegrove et al., 1965) caused by mixing of the atmosphere by the spectrum of non-breaking waves, although as we will see below, the effective wave diffusivity $K_{\rm Wave}$ arises from a spectrum of uncorrelated coherent wave motions, while classical diffusion arises from the completely random thermal motions of molecules and the random velocities of turbulent eddies. The third term is the chemical flux which arises from wave-induced perturbations in the constituent chemistry that are partially correlated with the vertical wind fluctuations (Gardner & Liu, 2016). The first two terms can be derived directly by applying Fick's First Law of Diffusion to the constituent mixing ratio (ρ_C/ρ_A) (see Equation B4), while the chemical flux is derived in terms of the species chemistry by Gardner and Liu (2016) and Gardner (2018). Missing from this expression are the diffusive fluxes associated with mixing by turbulence and the thermal motion of molecules, which are characterized by the eddy diffusivity K_{zz} and molecular diffusivity $K_{\rm Mole}$. For reader convenience, the key diffusivities discussed in the remainder of this section are defined in Appendix B.

$K_{\rm Wave}$ is approximately proportional to the Stokes drift velocity imparted to the atmosphere by the spectrum of waves (Gardner et al., 2019)

$$K_{\rm Wave} \simeq \frac{g}{N^2}\frac{\overline{w'\rho_A'}}{\overline{\rho}_A} = -\frac{g}{N^2}\left(\frac{\overline{w'T'}}{\overline{T}} - \frac{\overline{w'p'}}{\overline{p}}\right), \tag{2}$$

where p is the atmospheric pressure, N is the buoyancy frequency, $\overline{\mathrm{w}'\mathrm{p}'}$ is the gravity wave energy flux, and $\overline{w'T'}$ is the sensible heat flux. This expression for $K_{\rm Wave}$ is valid provided each wave in the spectrum obeys the gravity wave polarization and dispersion relations, satisfies mass conservation, and their vertical wavelengths satisfy $\lambda_z << 4\pi\mathrm{H}_{\mathrm{A}}$, where $H_{\rm A}$ is the atmospheric scale height, and $\frac{Var(\rho_A')}{\overline{\rho}_A^2} \sim \frac{Var(T')}{\overline{T}^2} \ll 1$, which is easily satisfied

in the mesopause region above Ft. Collins where Var(T′) ~ 60 K^2 and T ~ 200 K (She et al., 2022). By combining (1) and (2) the wave-driven constituent flux can also be written as

$$\overline{w'\rho_C'} = -\bar{\rho}_C\left(\frac{g}{R\overline{T}} - \frac{g}{C_p\overline{T}} + \frac{1}{\bar{\rho}_C}\frac{\partial\bar{\rho}_C}{\partial z}\right)K_{\text{Wave}} + \overline{w'\rho_C'}_{\text{Chemical}}. \tag{3}$$

Although K_{Wave} has units of diffusivity, atmospheric mixing caused by non-breaking waves is different than classical eddy and molecular diffusion because of the Stokes drift term. The environmental lapse rate ($-\partial T/\partial z$) in the classical diffusion term in Equation 1 is replaced by g/C_p in the wave mixing (diffusion) term in 3. K_{Wave} arises through the atmospheric mixing induced by the spectrum of propagating waves, which is fundamentally different than the mixing associated with the random velocity fluctuations caused by turbulence (described by K_{zz}) or the random thermal motions of atmospheric molecules (described by K_{Mole}). Each wave imparts an organized, non-random motion to the atmosphere even though the cumulative effect of the wave spectrum appears to be random (Gardner & Yang, 1998). While molecular and eddy diffusivities are always positive, K_{Wave} can be negative in regions where the wave spectrum is dominated by downward propagating waves so that the net energy flux is downward (Chu et al., 2021; Gardner et al., 2019).

The thermal diffusivity (K_H) is defined in terms of the vertical flux of potential temperature ($\overline{w'\theta'}$) and can be derived by applying Fick's First Law of Diffusion, which states that the diffusive flux of a substance or parameter (θ) is proportional to the concentration gradient and the constant of proportionality is the diffusivity,

$$K_H = -\left(\frac{\partial\bar{\theta}}{\partial z}\right)^{-1}\overline{w'\theta'} = -\frac{g}{N^2}\left(\frac{\overline{w'T'}}{\overline{T}} - \kappa\frac{\overline{w'p'}}{\bar{p}}\right) \tag{4}$$

where $\theta = T\left(\frac{p_0}{p}\right)^{\kappa}$, $\kappa = R/C_p$, $C_p = 1{,}003\ \text{m}^2\text{K}^{-1}s^{-2}$ is the specific heat at constant pressure, and $p_0 = 1{,}000$ hPa is the reference pressure. This formula for K_H also applies to turbulence fluctuations. However, for turbulence, the pressure fluctuations are negligible so that $(K_H)_{\text{Turbulence}} = K_{zz}$, where K_{zz} is the eddy diffusivity. Notice that K_H and K_{Wave} are similar, with both depending on the sensible heat and gravity wave energy fluxes. By combining (2) and (4), K_{Wave} can also be expressed as

$$K_{\text{Wave}} = K_H + \left(\frac{C_p}{R} - 1\right)K_E, \tag{5}$$

where for convenience we define K_E as the effective diffusivity associated with the gravity wave energy flux

$$K_E = \frac{g}{N^2}\kappa\frac{\overline{w'p'}}{\bar{p}}. \tag{6}$$

Unfortunately, the expressions for K_{Wave} and K_H given by 2 and 4 cannot be applied to the Colorado State University (CSU) data set because neither the sensible heat flux nor the energy flux were directly measured by the lidar. The sensible heat flux can be eliminated from these expressions by adopting the approach used by Gardner et al. (2019), which follows analyses first presented by Walterscheid (1981) and Liu (2000), who calculated the potential temperature flux by linearizing the thermodynamic equation. Potential temperature is a conserved quantity for an air parcel in adiabatic motion, that is, for motion in which there are no heat sources or sinks. We assume this condition applies to the mesopause region between 85 and 100 km above CSU. Hence, the potential temperature fluctuations, induced by gravity waves and turbulence, are described by the continuity equation for an incompressible flow, or equivalently, the convection-diffusion equation for heat flow in the presence of potential temperature gradients. The key result, given by Equation 17 in Gardner et al. (2019), is

$$K_H \simeq (K_{zz} + K_{\text{Wave}})\,\xi_{\text{inst}} \tag{7}$$

where

$$\xi_{\text{inst}} = \frac{\overline{(\partial\theta'/\partial z)^2}}{\left(\partial\bar{\theta}/\partial z\right)^2} \simeq \frac{\text{Var}(\partial T'/\partial z)}{\left(\Gamma_{\text{ad}} + \partial\overline{T}/\partial z\right)^2} \simeq \frac{\text{Var}(\partial u'/\partial z)}{N^2} = \overline{1/Ri}, \tag{8}$$

$\partial u'/\partial z$ is the vertical shear of the horizontal wind fluctuations, and Ri is the instantaneous Richardson number. By combining (5) and (7) we obtain

$$K_H = \frac{\xi_{\text{inst}}}{(1-\xi_{\text{inst}})}\left[K_{zz} + \left(\frac{C_p}{R} - 1\right)K_E\right] \tag{9}$$

and

$$K_{\text{Wave}} = \frac{1}{(1-\xi_{\text{inst}})}\left[\xi_{\text{inst}}K_{zz} + \left(\frac{C_p}{R} - 1\right)K_E\right]. \tag{10}$$

The instability parameter (ξ_{inst}) is the normalized lapse rate fluctuation variance, which for gravity wave perturbations, is approximately equal to the mean of the inverse Richardson number. It is a measure of the instability of the atmosphere through which the waves are propagating. Larger values correspond to a less stable atmosphere and for gravity waves ξ_{inst} is always less than one. In addition to its influence on K_{H} and K_{Wave}, ξ_{inst} also affects the constituent flux associated with eddy and molecular diffusion (Gardner et al., 2019)

$$\overline{\text{w}'\rho_{\text{C}}'}_{\text{Eddy+Mole}} = -\bar{\rho}_{\text{C}}\left(\frac{g}{\text{R}\overline{\text{T}}} + \frac{1}{\text{T}}\frac{\partial\overline{\text{T}}}{\partial z} + \frac{1}{\bar{\rho}_{\text{C}}}\frac{\partial\bar{\rho}_{\text{C}}}{\partial z}\right)(1+\xi_{\text{inst}})(\text{K}_{zz} + \text{K}_{\text{Mole}}). \tag{11}$$

K_{zz} is the eddy diffusivity generated by breaking waves and K_{Mole} is the molecular diffusivity for the constituent C. This expression is different from the classical formula because the diffusion is enhanced by the factor $(1+\xi_{\text{inst}})$. This enhancement arises because the waves perturb the species mixing ratio gradients, which increases the mixing associated with turbulence and the thermal motion of the constituent atoms (Gardner, 2018; Grygalashvyly et al., 2012). In the mesopause region at CSU, ξ_{inst} varies between about ¼ and ½ and does not exceed one. Hence, the impact of ξ_{inst} on K_{H} and K_{Wave} and on the enhancement of eddy and molecular diffusion is important.

The energy flux, and therefore K_{E}, can be written in terms of the normalized temperature variance by expressing the wave-driven p′ spectrum in terms of the T' spectrum, as originally suggested by Liu (2009) and generalized later by Gardner (2018). We use the expression for K_{E} derived by Chu et al. (2021) in the appendix of their paper and given by their Equation 10

$$K_E = \frac{g}{N^2}\kappa\frac{\overline{w'p'}}{\bar{p}} \simeq 8\sqrt{2}(1-2\alpha_{\text{down}})\frac{\Gamma_{\text{ad}}f}{\overline{T}}\left[\frac{\text{Var}(T')}{\left(\Gamma_{\text{ad}} + \partial\overline{\text{T}}/\partial z\right)^2}\right]^{3/2}, \tag{12}$$

where α_{down} is the fraction of gravity wave energy propagating downward and f is the inertial frequency. Waves can propagate downward if they are reflected from above, are ducted (e.g., Walterscheid & Hickey, 2009; Yu & Hickey, 2007), or are secondary waves generated above by the breaking of primary waves (e.g., Becker & Vadas, 2018). Numerous studies have shown that α_{down} can vary over a relatively wide range depending on location, altitude, and season. For example, Wang et al. (2005) analyzed extensive balloon sonde measurements over the U.S. and reported that on average ~50% of the gravity wave energy propagates downward in the troposphere and ~25% propagates downward in the lower stratosphere. Strelnikova et al. (2020) published Rayleigh lidar wind measurements made at ALOMAR, Norway (69.3°N, 16.0°E) between 30 and 80 km in the stratosphere and mesosphere. They reported that 32.2% of all the detected gravity waves propagated downward. Hu et al. (2002) employed a Na Doppler lidar to study gravity waves in the mesopause region between 84 and 104 km at the SOR, NM (35°N, SOR). SOR is located near Albuquerque, NM approximately 625 km almost due south of CSU. Only 15.6% of all waves observed in the MLT at SOR were propagating downward. Although the fraction of downward propagating gravity waves could become quite large, especially near regions experiencing significant wave dissipation and secondary wave generation (e.g., Chu et al., 2021), because we did not measure α_{down} at CSU, we used the value 15% in our calculations, which is comparable to the measured value at SOR. K_{H} and K_{Wave} given by 9 and 10 are quite sensitive to the values of α_{down} and K_{zz}, which may exhibit seasonal variations. Unfortunately, we are not aware of any measurements of the seasonal variations in α_{down} near CSU and measurements of the seasonal variations of K_{zz} are rare anywhere. However, when such information becomes available, it is straightforward to recompute K_{H} and K_{Wave} using the measured seasonal variations of Var(T'), Var($\partial T'/\partial z$), T, and N contained in this paper and in the companion paper (She et al., 2022).

Notice that K_E is proportional to the 3/2 power of the normalized temperature fluctuation variance,

$$\overline{\zeta^2} = \frac{\mathrm{Var}(T')}{\left(\Gamma_{ad} + \partial\overline{T}/\partial z\right)^2} \tag{13}$$

where ζ is the vertical displacement induced by the waves. For chemically active species, the wave-induced chemical flux ($\overline{w'\rho_C'}_{\mathrm{Chemical}}$) is also proportional to the normalized temperature variance (Gardner & Liu, 2016; Gardner et al., 2019) as is the gravity wave potential energy density per unit mass (E_{pm})

$$E_{pm} = \frac{g^2}{2N^2}\frac{\mathrm{Var}(T')}{\overline{T}^2} = \frac{N^2}{2}\frac{\mathrm{Var}(T')}{\left(\Gamma_{ad} + \partial\overline{\mathrm{T}}/\partial z\right)^2}. \tag{14}$$

Thus, the normalized temperature variance is an important parameter that is equal to the mean-square displacement imparted to the atmosphere by the spectrum of gravity waves. It is a measure of the atmospheric mixing caused by the waves. In the mesopause region at CSU, the normalized temperature variance ranges between about 0.4 and 1.5 km^2. According to (9) and (10), K_H and K_{Wave} are largest in regions where the atmospheric instability (ξ_{inst}) is large and wave mixing ($\overline{\zeta^2}$) is strong, namely in regions where the normalized temperature and lapse rate variances are both large. These are regions experiencing significant wave dissipation and breaking. In the following sections we characterize the seasonal variations of constituent and heat transport between 85 and 100 km above Ft. Collins, CO by deriving the normalized temperature and lapse variances, K_H, and K_{Wave} from the extensive CSU Na lidar data set.

3. Observations

The Na Doppler lidar, developed at CSU, employed the two- and three-frequency techniques to make measurements of temperature (T), Na density (ρ_{Na}), and radial wind profiles (v_R, requires three-frequencies) in the mesopause region (She & Yu, 1994; She et al., 1990). Observations began at CSU in Ft. Collins, CO (41°N, 105°W) during March 1990 and continued through March 2010. Although daytime measurement capabilities were ultimately developed for the instrument, only nocturnal observations are employed in this study. A total of 956 nights of observations were made during the 20-year period, that are roughly evenly distributed over the spring (236 nights), summer (229 nights), autumn (274 nights), and winter (217) seasons. Note, here we define the seasons as those time periods centered on the respective equinoxes and solstices. A more detailed description of this data set can be found in the CSU temperature and gravity wave trend and climatology papers (She et al., 2019, 2022).

For this study we are primarily interested in the temperature measurements and the statistics of the associated wave-driven temperature fluctuations. To minimize errors caused by photon noise, temperature profiles were derived by averaging the photon counts over Δt = 10 min and smoothing vertically with a 2 km full-width Hanning window (Krueger at al., 2015). The combined effects of temporal averaging and Hanning window smoothing yields temperature profiles with an effective vertical resolution equal to Δz = 1.5 km (see Appendix A). The wave-driven temperature fluctuations (T') were derived using the same approach described by Gardner and Liu (2007). A linear trend in time at each altitude was subtracted to suppress waves with periods longer than the observation period (mean ~8.2 hr) and then a linear trend in altitude at each time was subtracted to suppress waves with vertical wavelengths longer than ~20 km. The sample T' variance was then computed and T' outliers greater than ±3 standard deviations were rejected. The process was repeated until the sample variance converged to a stable value. Finally, the photon noise variance was estimated using the measured photon counts and subtracted from the total variance at each altitude to yield an unbiased estimate of the temperature fluctuation variance profile for each night of observations. The sample variance of the lapse rate fluctuations was also computed from the final T' samples (with outliers eliminated) and the estimated photon noise variance subtracted to yield an unbiased estimate of the lapse rate variance at each altitude.

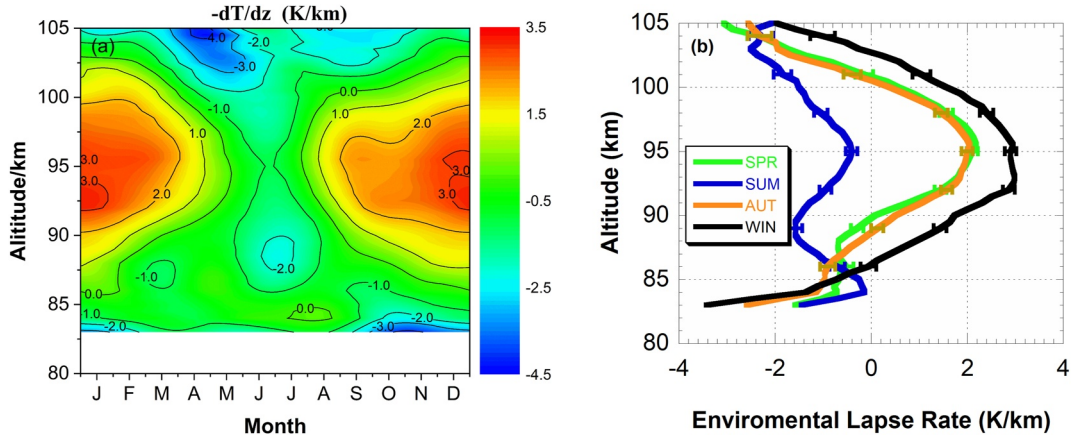

Figure 1. (a) Mean environmental lapse rate ($-\partial\overline{T}/\partial z$) structure derived from the 12-, 6-, 4-, and 3-month harmonic fit to nighttime lidar temperature observations made from March 1990 to 2010 at Ft. Collins, CO. (b) Seasonal mean profiles of the environmental lapse rate derived from the data plotted in (a).

4. Seasonal Variations of the Fundamental Thermal Structure

The mean atmospheric temperature and lapse rate profiles were computed for each of the 956 nights of observation and then fitted at each altitude to a harmonic model that included the annual mean, the 12 months annual oscillation and the 6 months (semi-annual), 4 and 3-month harmonics. The fitted temperature structure and the mesopause altitude and temperature are plotted in Figures 1a and 1c of the companion temperature and gravity wave climatology paper by She et al. (2022). These figures are included for reference in Figures S1 and S2 in Supporting Information S1, respectively. This structure is typical of that observed at other mid-latitude sites in the northern hemisphere. The mesopause is coldest and lowest in mid-summer near solstice and highest in mid-winter, also near solstice.

The mean environmental lapse rate ($-\partial\overline{T}/\partial z$) is plotted in color contour format in Figure 1a and the mean seasonal profiles are plotted in Figure 1b. The mean lapse rate is smallest during summer above 100 km in the lower thermosphere where it approaches −2.5 K/km. It is largest during winter between 92 and 96 km in the upper mesosphere where it is about +3 K/km. The mean lapse rate is used to calculate the square of the buoyancy frequency

$$N^2 = \frac{g}{\overline{T}}\left(\Gamma_{ad} + \partial\overline{T}/\partial z\right), \tag{15}$$

which is plotted in color contour format in Figure 2a the companion paper by She et al. (2022), see Figure S3 in Supporting Information S1). N^2 is a measure of the static stability of the atmosphere. The mesopause region exhibits the highest static stability in summer when the temperature is coldest and above 100 km in the lower thermosphere, where the mean environmental lapse rate is either near zero or negative (i.e., $\partial\overline{T}/\partial z$ is zero or positive). The lowest static stability occurs between 90 and 97.5 km during winter just below the mesopause where the lapse rate is positive ($\partial\overline{T}/\partial z$ is negative), and the temperature is relatively warm.

5. Seasonal Variations of Wave Activity and Wave-Driven Diffusivities

To evaluate K_H and K_{Wave}, we need to know the normalized temperature and lapse rate variances, which are derived from the CSU lidar data set, and K_{zz} which we obtained from the Whole Atmosphere Community Climate Model (WACCM, H.-L. Liu, National Center for Atmospheric Research, private communication). Because K_H and K_{Wave} are only weakly dependent on K_{zz}, to simplify calculations we used the annual mean K_{zz} profile that was derived from the WACCM gravity wave parameterization module for the MLT above CSU. The model K_{zz} profile is plotted in Figure 8b. The values range between 25 and 40 m^2s^{-1}, which are small, but reasonably consistent with other estimates inferred from rocket measurements of neutral density fluctuations (e.g., Lübken, 1997),

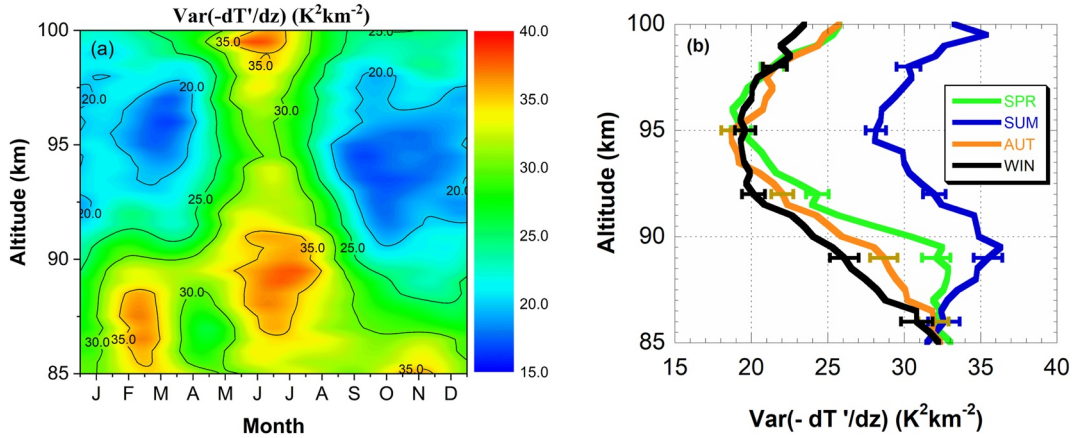

Figure 2. (a) Seasonal and altitude variations of the wave-induced lapse rate fluctuation variance Var(-$\partial T'/\partial z$), derived from the 12-, 6-, 4-, and 3-month harmonic fit to the Colorado State University nighttime lidar data. (b) Seasonal mean profiles of Var($-\partial T'/\partial z$) derived from the data plotted in (a).

lidar measurements of eddy heat fluxes (Guo et al., 2017), and satellite observations of atomic oxygen profiles (Swenson et al., 2018).

The inertial period at CSU is 18.4 hr and the buoyancy period in the mesopause region is about 5 min. Because of the finite vertical (Δz = 1.5 km) and temporal (Δt = 10 min) resolutions and the finite observation periods (mean ~8.2 hr) of the CSU lidar data set, the derived temperature fluctuations and their variances do not include contributions from the full gravity wave spectrum. Specifically, the temperature and lapse rate variances and the derived values of K_H and K_{Wave} reported here, do not include the thermal and constituent mixing contributed by the longer, inertial period waves with periods greater than the ~8 hr mean observation period, nor do they include contributions from waves with periods shorter than 20 min and vertical wavelengths smaller than $2\Delta z$ = 3 km (see Appendix A). The temperature fluctuations are dominated by waves with long periods and long wavelengths near the characteristic wavelength λ_z*, which is about 15 km at mesopause heights. The lapse rate fluctuations are dominated by waves with long periods and short vertical wavelengths up to $\lambda_b \sim 1$ km, which marks the transition from waves to turbulence. Because the vertical resolution of the CSU data set (Δz = 1.5 km) eliminates waves with wavelengths less than $2\Delta z$ = 3 km, it is necessary to correct the measured lapse rate variance by estimating the contributions from the shortest vertical wavelength waves and adding the estimate to the measured variance. By assuming that the temperature spectrum is proportional to m^{-3}, where m is the vertical wavenumber, the corrected the lapse rate variance is

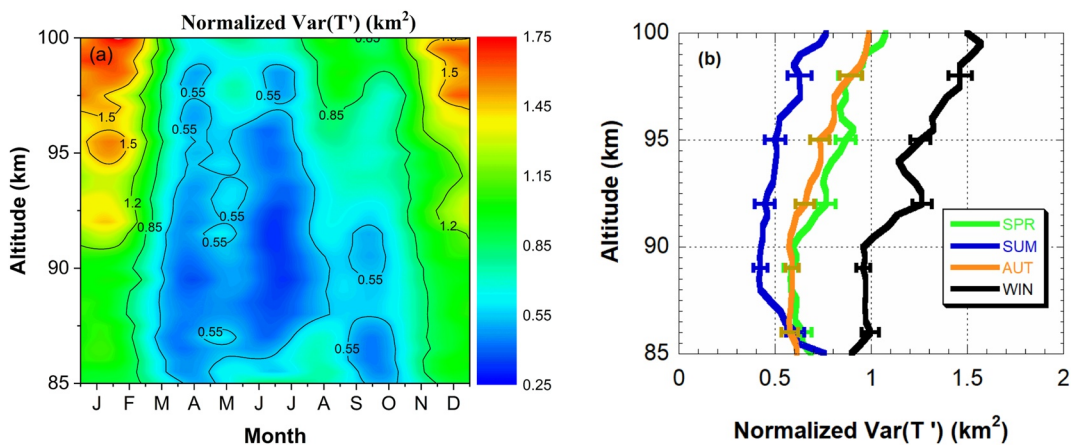

Figure 3. (a) Seasonal and altitude variations of the normalized temperature variance $\overline{\zeta^2} = Var(T') / \left(\Gamma_{ad} + \partial \overline{T}/\partial z\right)^2$. (b) Seasonal mean profiles of $\overline{\zeta^2}$ derived from the data plotted in (a).

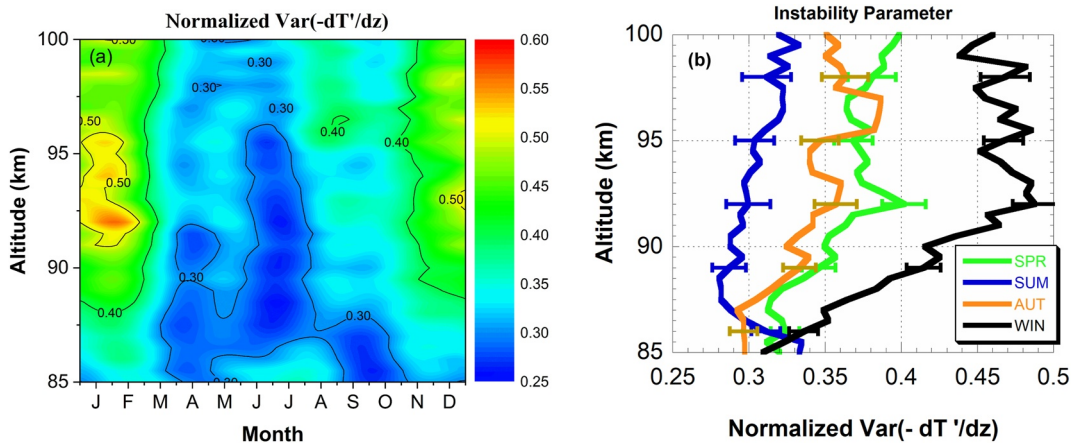

Figure 4. (a) Seasonal and altitude variations of the normalized lapse rate variance $\xi_{inst} = Var\left(-\partial T'/\partial z\right)/\left(\Gamma_{ad} + \partial\overline{T}/\partial z\right)^2$. (b) Seasonal mean profiles of ξ_{inst}derived from the data plotted in (a).

$$\text{Var}\left(\frac{\partial T'}{\partial z}\right) = \text{Var}\left(\frac{\partial T'}{\partial z}\right)_{\text{measured}} + \frac{1}{8}\ln\left(\frac{2\Delta z}{\lambda_b}\right)\left(\Gamma_{\text{ad}} + \frac{\partial\overline{T}}{\partial z}\right)^2 \simeq \text{Var}\left(\frac{\partial T'}{\partial z}\right)_{\text{measured}} + 0.14\left(\Gamma_{\text{ad}} + \frac{\partial\overline{T}}{\partial z}\right)^2. \quad (16)$$

The sample temperature and lapse rate fluctuation variances were computed for each night of observations and then fitted at each altitude to a harmonic model that included the annual mean plus the 12-, 6-, 4-, and 3-month oscillations. The fitted temperature variance is plotted in contour format in Figure 4a and the seasonal mean profiles are plotted in Figure 5a in She et al. (2022), see Figures S4 and S5 in Supporting Information S1). The uncertainties are derived directly from the harmonic fits to the nightly observations. Wave activity as characterized by Var(T′) is strongest in winter and summer and weakest during the spring and fall equinoxes. The values are comparable to those observed at the SOR, NM (Gardner & Liu, 2007), but the altitude variations are quite different (see Figure 9 below). Var(T′) profiles exhibit a local maxima near 90 km and local minima near 96 km at SOR but exhibit only local minima near 93.5 km at CSU. The corresponding data for the lapse rate variance is plotted in Figure 2. The lapse rate variance is strongest in summer when N^2, and hence the static stability of the atmosphere, is highest. The summer lapse rate variance profile is similar to that observed at SOR (Gardner & Liu, 2007) with a local maximum ~36 K^2km^{-2} near 90 km and a local minimum ~28 K^2km^{-2} near 95 km.

The key parameters for computing the wave-induced thermal (K_H) and constituent diffusivities (K_{Wave}) are the normalized temperature and lapse rate variances, which are plotted in Figures 3 and 4, respectively, and tabulated in Table 1. The normalized temperature variance is largest in winter where reaches 1.5 km^2 at the highest altitudes near the mesopause. It is smallest in summer with values less than half those observed in winter. Recall that the normalized temperature variance is approximately equal to the mean-square vertical displacement ($\overline{\zeta^2}$) imparted to the atmosphere by the spectrum of gravity waves. Thus, atmospheric mixing in the mesopause region at CSU is clearly strongest in winter, weakest in summer, with the spring and fall profiles falling approximately mid-way between these winter/summer extremes. Static stability (N^2) is also weakest in winter which suggests this is also a period of stronger wave dissipation. This is consistent with the seasonal variations of the normalized lapse rate variance plotted in Figure 4. Remember this parameter, also called the instability parameter (ξ_{inst}), is approximately equal to the mean of the inverse Richardson number. It is clearly largest in winter where it reaches values exceeding 0.45 above 90 km altitude and is smallest in summer with values ~0.30. The gravity wave potential energy per unit mass (E_{pm}), which is proportional to the normalized temperature variance (see (14)) is plotted in Figures 4c and 5b in She et al. (2022), see Figures S6 and S7 in Supporting Information S1). E_{pm}, which is a good proxy for the strength of gravity wave activity, is clearly largest in winter, when wave-driven mixing ($\overline{\zeta^2}$) and instability (ξ_{inst}) are also largest.

Contour plots and seasonal profiles of K_E, K_H, and K_{Wave} are plotted in Figures 5–7, respectively, while K_H and K_{Wave} are tabulated in Table 2. All three diffusivities exhibit strong annual oscillations with the largest values in winter. It is not surprising that K_E is also largest in winter and smallest in summer because of its dependence

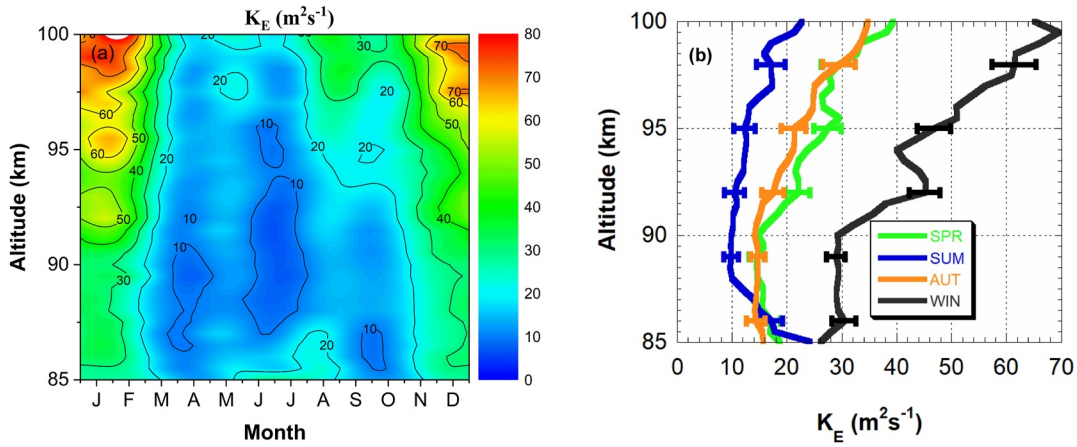

Figure 5. (a) Seasonal and altitude variations of the effective diffusivity K_E associated with the gravity wave energy flux. (b) Seasonal mean profiles of K_E derived from the data plotted in (a).

on the normalized temperature variance (see (12)). Above 90 km K_E varies by more than a factor of 3 between summer and winter. Because K_H and K_{Wave} also depend on ξ_{inst}, at the highest altitudes near the mesopause, the thermal and constituent diffusivities vary by about a factor of 4 between their summer minima and winter maxima. In summer when K_H is smallest, it is still larger than K_{zz} (see Figure 8b) while K_{Wave} is more than twice K_{zz} during summer and about 10 times larger near 100 km during winter. Wave-induced mixing and the subsequent heat and constituent transport is important throughout the year in the mesopause region above CSU, but wave mixing is especially significant in winter when wave activity is strongest and atmospheric stability is lowest.

6. Discussion

The seasonal variations of the wave-driven thermal (K_H) and constituent (K_{Wave}) diffusivities have been measured at two other mid-latitude sites, viz. The SOR near Albuquerque, NM (SOR, 34.96°N, 106.46°W) and the Andes Lidar Observatory at Cerro Pachón (CP), Chile (30.25°S, 70.74°W). The length of the observation periods and vertical resolutions are comparable at all three sites so the same region of the gravity wave spectrum was observed. Like CSU, both CP and SOR are located near significant mountain ranges and SOR is about 625 km south of CSU. Also, like CSU, the thermal diffusivities at CP (Figure 4a, Guo & Liu, 2021) and SOR (Figure 2b, Liu, 2009) exhibit strong annual oscillations with maxima in winter. The annual mean K_H profiles observed between 85 and 100 km at all three sites are plotted in Figure 8a. The corresponding annual mean K_{Wave} profiles are plotted in Figure 8b. The SOR data were taken from Table 1 in Gardner (2018) with K_{Wave} computed using

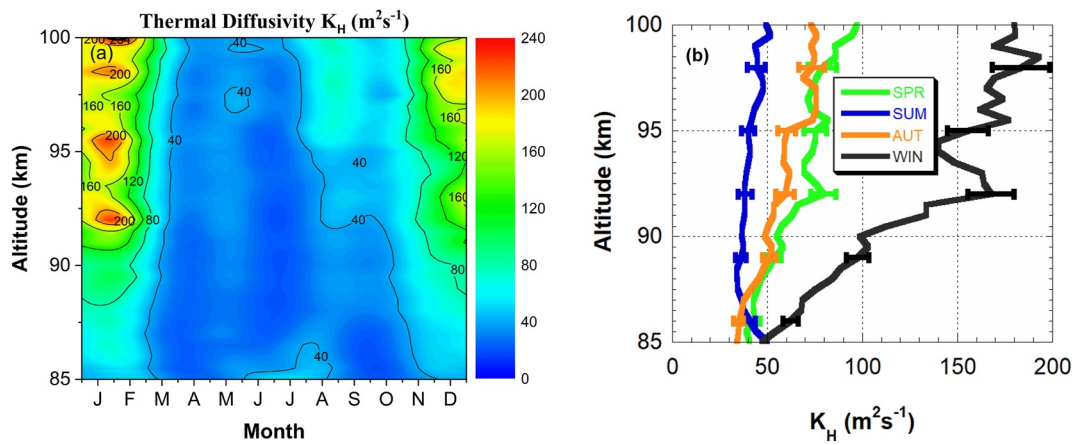

Figure 6. (a) Seasonal and altitude variations of the wave-induced thermal diffusivity K_H associated with the potential temperature flux. (b) Seasonal mean profiles of K_H derived from the data plotted in (a).

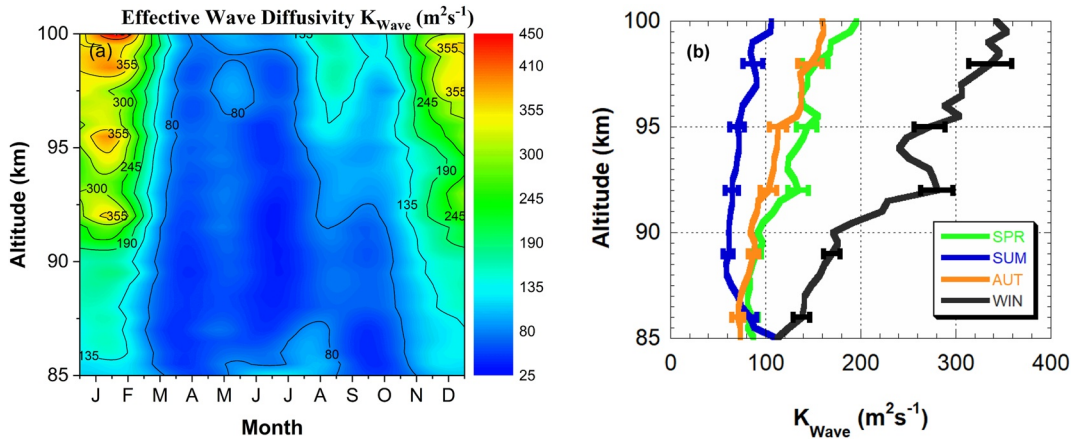

Figure 7. (a) Seasonal and altitude variations of the effective wave-induced constituent diffusivity K_{Wave}. (b) Seasonal mean profiles of K_{Wave} derived from the data plotted in (a).

Equations 4 and 5. The CP data were derived from the most recent observations reported by Guo and Liu (2021), who assumed that 15% of the waves were propagating downward. However, an unpublished hodograph analysis of ~1,200 gravity waves observed with the Na Doppler lidar at CP, suggests that 30.5% of the waves are propagating downward (Fabio Vargas, University of Illinois, private communications). The CP values of K_H and K_{Wave} plotted in Figure 8 were adjusted to reflect the larger value of α_{down} = 30.5% with K_{Wave} also computed using Equations 4 and 5.

The wave-induced K_H and K_{Wave} values (hundreds of m^2s^{-1}) at all three sites are much larger than the typical values observed for the turbulence-induced K_{zz} (tens of m^2s^{-1}) at mesopause heights. Although the latitudes and orography of the three sites are similar, the mean diffusivity profiles are quite different. K_H and K_{Wave} are largest at CP with relatively weak altitude variations, while the values are largest just below 90 km at SOR, but at CSU they increase with increasing altitude. The mean values for K_H (K_{Wave}) between 85 and 100 km are 268 m^2s^{-1} (287 m^2s^{-1}) at CP, 90 m^2s^{-1} (144 m^2s^{-1}) at SOR, and 72 m^2s^{-1} (136 m^2s^{-1}) at CSU. The diffusivities observed at CP and SOR were calculated from the measured sensible heat flux and temperature fluctuation variance profiles using Equations 2, 4 and 12. Because the sensible heat flux was not measured at CSU, the diffusivities were calculated from the measured temperature and lapse rate fluctuation variance profiles using Equations 8– Equations 10 and Equations 12. Recall that this latter approach is valid for purely adiabatic wave-induced motions in which there are no heat sources or sinks.

The diffusivity differences among these sites may reflect differences in wave activity and/or the wind and thermal characteristics of the background atmosphere through which the waves are propagating. The temperature fluctuation variance is a good proxy for wave activity. The annual mean Var(T′) profiles for all three sites are plotted in Figure 9. They are similar, although the CSU profile exhibits its largest values of 68 K^2 at 85 km and 70 K^2 at 100 km and its smallest value of 41 K^2 at 93.5 km. The SOR profile increases with increasing altitude from 56 K^2 at 85 km, reaching a local maximum of 72 K^2 at 90 km. Var(T′) then decreases above 90 km reaching a local minimum of 47 K^2 at 96 km before increasing above 96 km, reaching a value of almost 80 K^2 at 100 km. Gardner and Liu (2007) noted that the annual mean heat flux measured at SOR was also maximum and downward near 90 km, indicating that this was a region of significant wave dissipation and breaking (Walterscheid, 1981). They hypothesized that the reduction in temperature variance above 90 km is caused by significant wave energy being dissipated as turbulence between 90 and 96 km. In addition, this is probably a region of strong secondary wave generation as modeled by Vadas and Becker (2019) and inferred by Chu et al. (2021) at McMurdo, Antarctica. Above 96 km at SOR the heat flux is near zero indicating weak dissipation, so the wave amplitudes and Var(T′) again increase between 96 and 100 km in response to decreasing atmospheric density. The CP profile exhibits a similar behavior, although the local maximum at 91 km (58 K^2) and the shallow local minimum at 93.5 km (56 K^2) are not as pronounced as those observed at SOR. In other words, the CP Var(T′) profile exhibits a broad plateau between ~88 and ~94 km where dissipation is just sufficient to balance the wave amplitude growth

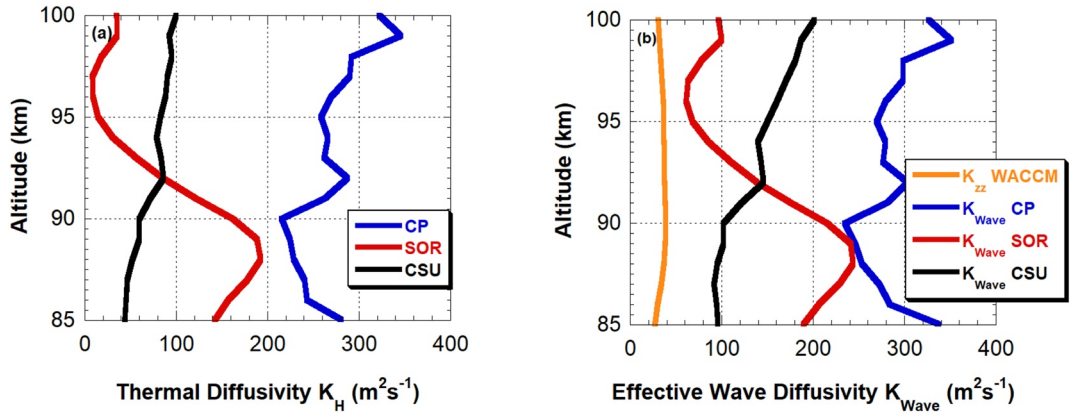

Figure 8. (a) Annual mean profiles of the wave-driven thermal diffusivity (K_H) measured at Ft. Collins Colorado State University (CSU), Cerro Pachón (CP), and the Starfire Optical Range (SOR). (b) Annual mean profiles of the effective wave-induced constituent diffusivity (K_{Wave}) measured at CSU, CP, and SOR and eddy diffusivity (K_{zz}) derived from the Whole Atmosphere Community Climate Model (WACCM) gravity wave parameterization.

associated with decreasing atmospheric density. Notice that the local minima for the three sites all occur at similar heights between 93.5 and 96 km.

It's possible that significant wave dissipation and breaking begins below 85 km at CSU in contrast to about 90 km at SOR and CP, which could explain the differences in the behavior of the Var(T′) profiles. In fact, winter observations of Var(T′) at the high latitude site McMurdo, Antarctica (77.84°S, 166.67°E) exhibit a local maximum of 110 K^2 at 84 km and a local minimum of 60 K^2 at 94 km (Chu et al., 2021, Figure 3a). These authors note that this behavior of the Var(T′) profile is nearly identical to that modeled by Vadas and Becker (2019) over the Southern Andes where the local maximum at 84 km corresponds to a region of significant wave breaking, leading to the generation of secondary gravity waves, which can propagate both upward and downward. The McMurdo observations include the effects of the long inertial period waves while the CSU, SOR, and CP observations do not. This accounts for the larger Var(T′) values at McMurdo. However, the mean observation periods (~7–8 hr) and vertical resolutions (~1 km) at CSU, SOR and CP are comparable so that the corresponding K_H and K_{Wave} values correspond to the same portion of the gravity wave spectrum.

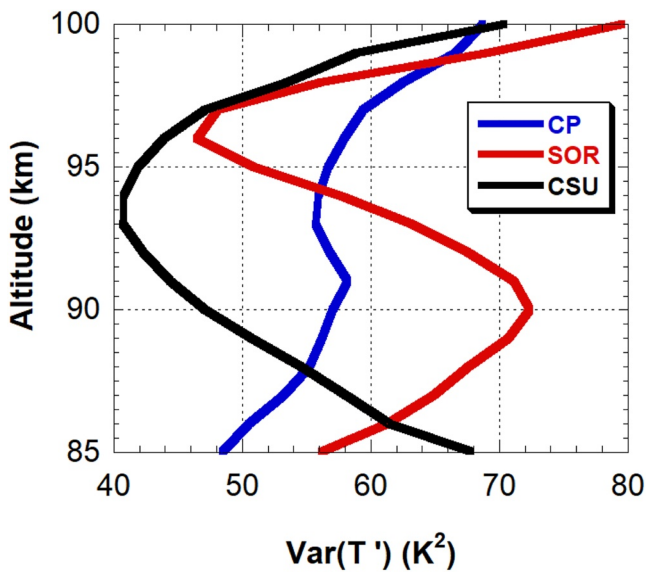

Figure 9. Annual mean profiles of the wave-driven temperature fluctuation variances measured at Ft. Collins Colorado State University (CSU), Cerro Pachón (CP), and the Starfire Optical Range (SOR).

By comparing the theoretical expression for the vertical flux of atomic Na given by 1 with the measured Na flux at McMurdo, Chu et al. (2021) also show that the fraction of wave energy propagating downward (α_{down}) varies in altitude, with values approaching and potentially exceeding 50% in regions of strong wave dissipation. The K_H and K_{Wave} profiles at CP, SOR, and CSU were calculated by assuming different but constant values of α_{down}. Because the temperature fluctuation variances are comparable at CP, SOR, and CSU, we believe that differences in the background wind and thermal structures at these sites, which affect atmospheric stability, wave dissipation, and the spectra of upward and downward propagating waves, are most likely responsible for the differences in K_H and K_{Wave} observed in Figure 8.

The CSU observations reported here were conducted exclusively at night. Because waves generated by convection are primarily a daytime phenomenon, and the daytime temperature structure can be considerably different because of tides and insolation (e.g., see Figure 14 in States & Gardner, 2000), the normalized T and lapse rate fluctuation variances are expected to be different from the nighttime values. This will alter the profiles of K_H and K_{Wave} computed according to Equations 8– Equations 10 and Equations 12 and so the daytime heat and constituent transport is expected to differ from nighttime values. For example, Figure 10 in Smith et al. (2010) shows clear differences

Table 1
Seasonal[a] and Annual Means of the Normalized Temperature and Lapse Rate Variances

Quantity	$\frac{Var(T')}{(\Gamma_{ad}+\partial\overline{T}/\partial z)^2}$ (km^2)					$\frac{Var(-\partial T'/\partial z)}{(\Gamma_{ad}+\partial\overline{T}/\partial z)^2}$				
Altitude (km)	Spring mean	Summer mean	Autumn mean	Winter mean	Annual mean	Spring mean	Summer mean	Autumn mean	Winter mean	Annual mean
100	1.07	0.768	0.990	1.50	1.07	0.399	0.320	0.351	0.460	0.380
99	0.964	0.631	0.968	1.52	1.01	0.387	0.314	0.350	0.438	0.371
98	0.890	0.628	0.893	1.46	0.958	0.381	0.312	0.363	0.468	0.379
97	0.871	0.632	0.806	1.39	0.913	0.365	0.322	0.387	0.455	0.381
96	0.845	0.523	0.808	1.31	0.864	0.367	0.319	0.384	0.465	0.383
95	0.868	0.500	0.732	1.26	0.829	0.369	0.304	0.347	0.467	0.369
94	0.795	0.503	0.737	1.14	0.787	0.378	0.308	0.340	0.465	0.370
93	0.748	0.490	0.683	1.23	0.777	0.374	0.297	0.361	0.486	0.377
92	0.764	0.448	0.655	1.26	0.770	0.402	0.300	0.357	0.488	0.384
91	0.678	0.437	0.597	1.09	0.690	0.363	0.296	0.342	0.465	0.364
90	0.588	0.424	0.574	0.959	0.629	0.349	0.288	0.324	0.415	0.342
89	0.582	0.423	0.589	0.959	0.631	0.346	0.287	0.333	0.415	0.344
88	0.583	0.424	0.589	0.971	0.634	0.321	0.282	0.315	0.384	0.324
87	0.608	0.526	0.580	0.966	0.662	0.312	0.288	0.292	0.349	0.309
86	0.644	0.603	0.578	0.996	0.695	0.324	0.311	0.297	0.336	0.316
85	0.688	0.767	0.615	0.896	0.733	0.321	0.333	0.297	0.309	0.314
Mean	**0.762**	**0.545**	**0.712**	**1.18**	**0.791**	**0.360**	**0.305**	**0.340**	**0.429**	**0.357**

[a]Seasonal means were computed over time periods centered on the respective equinoxes and solstices.

in the seasonal/intra-annual variation of atomic oxygen in the upper mesosphere, depending on whether daytime or nighttime observations are employed. These differences may be partially associated with differences in wave-induced transport between night and day. Obviously, a more complete description of wave transport is desired and could be obtained by making high resolution T measurements during the daytime.

In a series of recently published papers, Swenson and colleagues have used a different approach to characterize atmospheric mixing in the mesopause region (Swenson et al., 2018, 2019; 2021). They employed global satellite measurements of atomic O and other key species made by the Sounding of the Atmosphere using Broadband Emission Radiometry instrument (Russell et al., 1999; Smith et al., 2010) to derive the vertical O flux profile required to balance the chemical loss of O. Their 1-D approach ignores horizontal transport, which they justify by computing zonal mean fluxes that are averaged over broad latitudinal bands. They then use the derived O fluxes, in combination with the classical diffusion equation (second term on the right-hand-side of 1), to compute the diffusivity profile required to produce the O flux profile. In addition to neglecting horizontal transport, they also neglect the wave-induced chemical flux of O (third term on the right-hand-side of 1), which is justified above 85–90 km because it is very small in comparison to the diffusive flux (Appendix B; Gardner, 2018). Plotted in Figure 10a is the annual mean diffusivity profile derived by Swenson et al. (2021) for the northern hemisphere, averaged between 15°N and 55°N (denoted K_{S21}). Also plotted for comparison is the annual mean profile of K_{Wave} at CSU (41°N). The major difference is that the K_{S21} exhibits a pronounced minimum at 90 km, while the CSU K_{Wave} profile generally increases with increasing altitude between 85 and 100 km.

Although the diffusivity values are comparable, the differences probably reflect the fact that K_{Wave} corresponds to a single site at 41°N while K_{S21} represents a zonal average over a 40° latitude band centered at 35°N. Colorado State University is a mountain site while the K_{S21} global average is biased more toward ocean topography. The annual mean K_H and K_{Wave} profiles at CSU, CP, and SOR, that are plotted in Figure 8, illustrate that wave-driven diffusivities can vary significantly with location even when the latitude is similar. It's also important to note that

Table 2
Seasonal[a] and Annual Means of Thermal (K_H) and Constituent (K_{Wave}) Diffusivities

Quantity	Wave-induced thermal diffusivity K_H (m^2s^{-1})					Wave-induced constituent diffusivity K_{Wave} (m^2s^{-1})				
Altitude (km)	Spring mean	Summer mean	Autumn mean	Winter mean	Annual mean	Spring mean	Summer mean	Autumn mean	Winter mean	Annual mean
100	97.5	49.6	73.2	180	97.8	196	107	160	343	197
99	85.5	43.4	73.2	169	90.9	169	86.3	157	334	183
98	79.0	44.3	73.5	183	92.8	152	87.0	147	337	177
97	73.6	48.0	75.8	165	88.9	144	91.4	138	306	166
96	73.1	43.3	75.9	162	86.9	140	76.1	138	289	158
95	75.4	39.9	60.4	156	80.8	144	70.6	113	273	147
94	73.7	41.2	59.1	140	76.9	133	72.3	112	240	137
93	69.6	39.1	61.8	163	81.3	123	69.1	109	273	140
92	79.6	38.5	59.5	168	84.0	134	64.7	103	280	142
91	63.1	38.1	53.3	134	70.3	109	63.5	91.0	222	119
90	55.1	36.5	48.6	98.5	58.6	91.9	61.1	83.9	171	100
89	53.8	36.3	51.1	97.6	58.8	90.1	61.0	87.8	170	101
88	46.7	34.2	45.4	84.2	51.8	83.0	59.1	82.1	157	93.9
87	42.9	36.5	37.7	68.5	45.7	81.8	71.4	73.7	141	90.4
86	43.1	40.9	35.1	62.4	44.7	85.7	83.8	71.0	138	93.0
85	41.1	50.7	33.6	46.7	42.5	88.3	112	73.2	112	95.0
Mean	**65.8**	**41.3**	**57.3**	**130**	**72.0**	**123**	**72.3**	**109**	**237**	**134**

[a]Seasonal means were computed over time periods centered on the respective equinoxes and solstices.

K_{S21} does not distinguish between K_{Wave}, which arises from the mixing associated with a spectrum of coherent, organized wave motions, and K_{zz}, which arises from mixing associated with the incoherent random motions caused by turbulence. In other words, Swenson and colleagues also ignore the wave-driven Stokes drift (first term on the right-hand-side of 1), which can be important, especially in regions of significant wave dissipation. Of

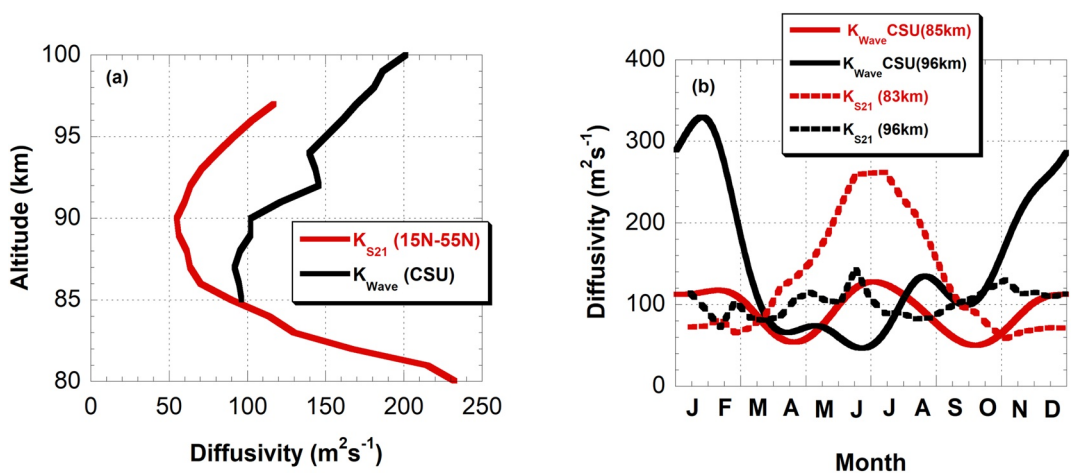

Figure 10. (a) Plots of the annual mean diffusivity profile (K_{S21}) derived from global observations of atomic O and the annual mean wave diffusivity (K_{Wave}) derived from the Colorado State University (CSU) Na lidar observations of temperature. (b) Plots of the seasonal variations of diffusivity (K_{S21}) derived from global observations of atomic O at 83 km (red dotted curve) and 96 km (black dotted curve) and the annual mean wave-induced constituent diffusivity (K_{Wave}) derived from the CSU Na lidar observations of temperature at 85 km (red solid curve) and 96 km (black solid curve).

course, K_{Wave} only reflects wave-induced mixing, while K_{S21} includes the combined effects of waves and turbulence on the diffusion of O and is generally expected to be larger than K_{Wave} at a specific location and time of year.

The seasonal variations of K_{S21} and the CSU K_{Wave} are plotted versus month in Figure 10b. The CSU data exhibit strong annual oscillations at 96 km with the maximum values for $K_{Wave} \sim 290$ m^2s^{-1} during winter and minimum values $\sim$75 m^2s^{-1} during summer. At 96 km K_{S21} is essentially constant throughout the year with values $\sim$100 m^2s^{-1}. At 85 km K_{Wave} is essentially constant throughout the year with values $\sim$100 m^2s^{-1}, while at 83 km K_{S21} exhibits a strong annual oscillation with maximum values $\sim$250 m^2s^{-1} during summer and minimum values $\sim$75 m^2s^{-1} during winter. Although the average values of CSU K_{Wave} and K_{S21} are similar, the seasonal variations are quite different. Again, we believe these differences are largely a consequence of the extensive geographical averaging used to derive K_{S21}, while K_{Wave} is derived from measurements made at a single mountain site.

7. Conclusions

The multi-decade temperature observations made at CSU in Ft. Collins, CO have been used to characterize the seasonal variations of gravity wave-driven, atmospheric mixing in the mesopause region between 85 and 100 km altitude. The vertical displacement fluctuations induced by the spectrum of waves contribute to significant vertical mixing of the atmosphere, which leads to the vertical transport of heat and constituents via a process similar, but not identical, to classical diffusion. The thermal (K_H) and constituent diffusivities (K_{Wave}) were derived by assuming that the wave-induced motions were purely adiabatic (so that 7 applies) and that the fraction of downward propagating waves was constant (15%) in altitude and season. The results incorporate mixing by waves with periods shorter than the mean observation period ($\sim$8.2 hr) and so they exclude the impact of longer inertial period waves. Both K_H and K_{Wave} at CSU are larger than the modeled eddy diffusivity (K_{zz}), which suggests that atmospheric mixing by non-breaking gravity waves is an important process in the upper atmosphere at this site. K_H and K_{Wave} exhibit strong annual oscillations with maxima in winter, which increase significantly with increasing altitude.

The CSU diffusivities are similar to those observed at CP, Chile and SOR, NM and derived from satellite observations of atomic O. At CP and SOR K_H also exhibits annual oscillations with maxima in winter (Guo & Liu, 2021; Liu, 2009). Satellite observations of O suggest that the total diffusivity induced by waves and turbulence only exhibit strong annual oscillations below 85 km with the maximum in summer (Swenson et al., 2021). These discrepancies in seasonal behavior are puzzling and may reflect differences in wave sources at these sites and the different approaches employed to derive the wave diffusivities. Even so, it should now be clear that heat and constituent transport by unresolved, non-breaking waves is an important process that needs to be incorporated in global chemistry models to accurately characterize the upper atmosphere. This is potentially straightforward. One simply needs to derive the wave-induced Var(T′) profile from the gravity wave parameterization employed by the model, and use (10) to compute K_{Wave}, which is then added to the eddy and molecular diffusivities calculated by the model. However, this change is likely to have other important impacts on model predictions, that will need to be addressed. For example, because K_{Wave} can be much larger than K_{zz} and K_{Mole}, incorporating K_{Wave} in the model will increase the transport of CO_2 upward above $\sim$75 km and O downward below $\sim$110 km. This will increase the radiative cooling by CO_2 and chemical heating by O, which in turn will impact the thermal balance and hence temperature of the MLT. Resolving such consequences should lead to a better understanding of the chemistry and dynamics of the Earth's upper atmosphere.

Appendix A

The CSU lidar data were smoothed vertically with a Hanning window function given by

$$w_{Hann}(z) = \frac{1}{2}\left[1 + \cos\left(\frac{2\pi z}{\Delta z}\right)\right] \quad -\frac{\Delta z}{2} \le z \le \frac{\Delta z}{2} \tag{A1}$$

where $\Delta z = 2$ km is the full width of the window. The magnitude squared of the Fourier transform of the Hanning window is

$$|W_{Hamm}(m)|^2 = \left(\frac{\Delta z}{2}\right)^2 \left[\frac{\sin(m\Delta z/2)}{m\Delta z/2}\right]^2 \left[\frac{\pi^2}{(m\Delta z/2)^2 - \pi^2}\right]^2 \tag{A2}$$

where m is the vertical wavenumber. This function attenuates the T′ and ∂T′/∂z m-spectra at the higher vertical wavenumbers. Furthermore, when the T′ fluctuations are filtered temporally with a cutoff frequency of $\omega_{max} \approx 2\pi/20$ min that is smaller than N, the m-spectra are also attenuated at the higher wavenumbers with this window function (Gardner, 1994)

$$|W_{\omega_{max}}(m)|^2 = 1 - \left(\frac{m}{m_{max}}\right)^4 \quad \text{where} \quad m_{max} \approx m_b\sqrt{\frac{\omega_{max}}{N}}. \tag{A3}$$

We define the 3-dB cutoff wavenumber $m_{1/2}$ as the solution to

$$\begin{aligned}\frac{1}{2} &= \frac{|W_{\text{Hann}}\left(m_{1/2}\right)|^2 |W_{\omega_{max}}\left(m_{1/2}\right)|^2}{|W_{\text{Hann}}(0)|^2 |W_{\omega_{max}}(0)|^2} \\ &= \left[\frac{\sin\left(m_{1/2}\Delta z/2\right)}{\left(m_{1/2}\Delta z/2\right)}\right]^2 \left[\frac{\pi^2}{\left(m_{1/2}\Delta z/2\right)^2 - \pi^2}\right]^2 \left[1 - \left(\frac{m_{1/2}\Delta z/2}{m_{max}\Delta z/2}\right)^4\right].\end{aligned} \tag{A4}$$

Solving this equation with $\lambda_b \approx 1$ km, we obtain $\lambda_{1/2} \approx 3$ km which means the effective vertical resolution of the CSU data is ~1.5 km.

Appendix B

The thermal diffusivity is defined in terms of the vertical flux of potential temperature. By applying Fick's First Law of Diffusion and the definition of potential temperature, we obtain

$$K_H = -\left(\frac{\partial\overline{\theta}}{\partial z}\right)^{-1}\overline{w'\theta'} = -\frac{g}{N^2}\left(\frac{\overline{w'T'}}{\overline{T}} - \frac{R}{C_p}\frac{\overline{w'p'}}{\overline{p}}\right) \tag{B1}$$

where

$$\frac{\partial\overline{\theta}}{\partial z} = \overline{\theta}\left(\frac{1}{\overline{T}}\frac{\partial\overline{T}}{\partial z} - \frac{R}{C_p}\frac{1}{\overline{p}}\frac{\partial\overline{p}}{\partial z}\right) = \overline{\theta}\frac{N^2}{g}. \tag{B2}$$

These equations apply for both gravity waves and turbulence, however for turbulence the pressure fluctuations are negligible, so that K_{zz} is defined as

$$K_{zz} = (K_H)_{\text{Turbulence}} = -\frac{g}{N^2}\frac{\left(\overline{w'T'}\right)_{\text{Turbulence}}}{\overline{T}}. \tag{B3}$$

The effective wave diffusivity is defined in terms of the vertical flux of the species mixing ratio (ρ_C/ρ_A). By ignoring the chemical flux and applying Fick's First Law of Diffusion, we obtain

$$K_{\text{Wave}} = -\left[\frac{\partial}{\partial z}\left(\frac{\overline{\rho}_C}{\overline{\rho}_A}\right)\right]^{-1}\overline{w'\left(\frac{\rho_C}{\rho_A}\right)'} = \left(\frac{1}{\overline{\rho}_C}\frac{\partial\overline{\rho}_C}{\partial z} - \frac{1}{\overline{\rho}_A}\frac{\partial\overline{\rho}_A}{\partial z}\right)^{-1}\left(\frac{\overline{w'\rho_A'}}{\overline{\rho}_A} - \frac{\overline{w'\rho_C'}}{\overline{\rho}_C}\right). \tag{B4}$$

By rearranging terms it is trivial to show that (B4) is identical to (1) when the chemical flux is ignored. K_{Wave} is derived by solving the continuity equation for ρ_C', where the perturbations are induced by gravity waves (Gardner & Shelton, 1985; Gardner et al., 2019).

$$K_{\text{Wave}} \simeq \frac{g}{N^2}\frac{\overline{w'\rho_A'}}{\overline{\rho}_A} = -\frac{g}{N^2}\left(\frac{\overline{w'T'}}{\overline{T}} - \frac{\overline{w'p'}}{\overline{p}}\right) \tag{B5}$$

This solution is valid for perturbations induced by the full spectrum of gravity waves provided each wave satisfies mass conservation, obeys the polarization and dispersion relations, and $\lambda_z << 4\pi H_A$ where H_A is the atmospheric

scale height. For mathematical convenience we define the effective diffusivity associated with the gravity wave energy flux as

$$K_E = \frac{g}{N^2}\frac{R}{C_p}\frac{\overline{w'p'}}{\overline{p}}. \quad \text{(B6)}$$

Data Availability Statement

The nightly mean and high-resolution CSU Na lidar temperature data (1990–2010) are available, respectively, at http://millstonehill.haystack.mit.edu/ and https://digitalcommons.usu.edu/all_datasets/54/.

Acknowledgments
We are grateful to Fabio A. Vargas of the University of Illinois for providing the hodograph analysis of the Cerro Pachón (CP) gravity wave measurements, to Alan Z. Liu at Embry-Riddle Aeronautical University for providing the CP sensible heat and potential temperature flux measurements, to Gary R. Swenson at the University of Illinois for providing the diffusivities derived from satellite observations of atomic O, and to David A. Krueger at Colorado State University(CSU) for his help with the harmonic analysis of the CSU temperature data. This work was partially supported by National Science Foundation grant AGS-2029162 and by the Strategic Priority Research Program of Chinese Academy of Sciences grant XDA17010303.

References

Becker, E., & Vadas, S. L. (2018). Secondary gravity waves in the winter mesosphere: Results from a high-resolution global circulation model. *Journal of Geophysical Research: Atmospheres*, *123*(5), 2605–2627. https://doi.org/10.1002/2017JD027460

Chu, X., Gardner, C. S., Li, X., & Lin, C. Y.-T. (2021). Vertical transport of sensible heat, and meteoric Na by the complete temporal spectrum of gravity waves in the MLT above McMurdo (77.84°, 166.67°E) Antarctica. *Journal of Geophysical Research: Atmospheres*, 2021JD035728RR.

Colegrove, F. D., Hanson, W. B., & Johnson, F. S. (1965). Eddy diffusion and oxygen transport in the lower thermosphere. *Journal of Geophysical Research*, *70*(19), 4931–4941. https://doi.org/10.1029/JZ070i019p04931

Coy, L., Fritts, D. C., & Weinstock, J. (1986). The Stokes drift due to vertically propagating internal gravity waves in a compressible atmosphere. *Journal of the Atmospheric Sciences*, *43*(22), 2636–2643. https://doi.org/10.1175/1520-0469(1986)043<2636:TSDDTV>2.0.CO;2

Gardner, C. S. (1994). Diffusive filtering theory of gravity wave spectra in the atmosphere. *Journal of Geophysical Research*, *99*(D10), 20601–20622. https://doi.org/10.1029/94JD00819

Gardner, C. S. (2018). Role of wave-induced diffusion and energy flux in the vertical transport of atmospheric constituents in the mesopause region. *Journal of Geophysical Research: Atmospheres*, *123*(12), 6581–6604. https://doi.org/10.1029/2018JD028359

Gardner, C. S., Guo, Y., & Liu, A. Z. (2019). Parameterizing wave-driven vertical constituent transport in the upper atmosphere. *Earth and Space Science*, *6*, 904–913. https://doi.org/10.1029/2019EA000625

Gardner, C. S., & Liu, A. Z. (2007). Seasonal variations of the vertical fluxes of heat and horizontal momentum in the mesopause region at Starfire Optical Range, New Mexico. *Journal of Geophysical Research*, *112*(D9), D09113. https://doi.org/10.1029/2005JD006179

Gardner, C. S., & Liu, A. Z. (2010). Wave-induced transport of atmospheric constituents and its effect on the mesospheric Na layer. *Journal of Geophysical Research*, *115*(D20), D20302. https://doi.org/10.1029/2010JD014140

Gardner, C. S., & Liu, A. Z. (2016). Chemical transport of neutral atmospheric constituents by waves and turbulence: Theory and observations. *Journal of Geophysical Research: Atmospheres*, *121*, 494–520. https://doi.org/10.1002/2015JD023145

Gardner, C. S., & Shelton, J. D. (1985). Density response of neutral atmospheric layers to gravity wave perturbations. *Journal of Geophysical Research*, *90*(A2), 1745–1754. https://doi.org/10.1029/JA090iA02p01745

Gardner, C. S., & Yang, W. (1998). Measurements of the dynamical cooling rate associated with the vertical transport of heat by dissipating gravity waves in the mesopause region at the Starfire Optical Range, New Mexico. *Journal of Geophysical Research*, *103*(D14), 16909–16926. https://doi.org/10.1029/98JD00683

Grygalashvyly, M., Becker, E., & Sonnemann, G. R. (2012). Gravity wave mixing and effective diffusivity for minor chemical constituents in the mesosphere/lower thermosphere. *Space Science Reviews*, *168*(1–4), 333–362. https://doi.org/10.1007/s11214-011-9857-x

Guo, Y., & Liu, A. Z. (2021). Seasonal variation of vertical heat and energy fluxes due to dissipating gravity waves in the mesopause region over the Andes. *Journal of Geophysical Research: Atmospheres*, *126*(3), e2020JD033825. https://doi.org/10.1029/2020JD033825

Guo, Y., Liu, A. Z., & Gardner, C. S. (2017). First Na lidar measurements of turbulence heat flux, thermal diffusivity and energy dissipation rate in the mesopause region. *Geophysical Research Letters*, *44*, 5782–5790. https://doi.org/10.1002/2017GL073807

Hickey, M. P., Walterscheid, R. L., & Philip, P. G. (2000). Secular variations of atomic oxygen in the mesopause region induced by transient gravity wave packets. *Geophysical Research Letters*, *27*(21), 3599–3602. https://doi.org/10.1029/2000GL011953

Hu, X., Liu, A. Z., Gardner, C. S., & Swenson, G. R. (2002). Characteristics of quasi-monochromatic gravity waves observed with lidar in the mesopause region at Starfire Optical Range, NM. *Geophysical Research Letters*, *29*(24), 2169. https://doi.org/10.1029/2002GL014975

Krueger, D. A., She, C.-Y., & Yuan, T. (2015). Retrieving mesopause temperature and line-of-sight wind from full-diurnal-cycle Na lidar observations. *Applied Optics*, *54*(32), 9469–9489. https://doi.org/10.1364/AO.54.009469

Liu, A. Z. (2009). Estimate eddy diffusion coefficients from gravity wave vertical momentum and heat fluxes. *Geophysical Research Letters*, *36*(8), L08806. https://doi.org/10.1029/2009GL037495

Liu, A. Z., & Gardner, C. S. (2004). Vertical dynamical transport of mesospheric constituents by dissipating gravity waves. *Journal of Atmospheric and Solar-Terrestrial Physics*, *66*(3–4), 267–275. https://doi.org/10.1016/j.jastp.2003.11.002

Liu, A. Z., & Gardner, C. S. (2005). Vertical heat and constituent transport in the mesopause region by dissipating gravity waves at Maui, Hawaii (20.7°N), and Starfire Optical Range, New Mexico (35°N). *Journal of Geophysical Research*, *110*(D9), D09S13. https://doi.org/10.1029/2004JD004965

Liu, H.-L. (2000). Temperature changes due to gravity wave saturation. *Journal of Geophysical Research*, *105*(D10), 12329–12336. https://doi.org/10.1029/2000JD900054

Liu, H.-L. (2021). Effective vertical diffusion by atmospheric gravity waves. *Geophysical Research Letters*, *48*(1), e2020GL091474. https://doi.org/10.1029/2020GL091474

Lübken, F.-J. (1997). Seasonal variation of turbulent energy dissipation rates at high latitudes as determined by in situ measurements of neutral density fluctuations. *Journal of Geophysical Research*, *102*(D12), 13441–13456. https://doi.org/10.1029/97JD00853

Russell, J. M., III, Mlynczak, M. G., Gordley, L. L., Tansock, J., & Esplin, R. (1999). An overview of the SABER experiment and preliminary calibration results. *Proceedings of SPIE The International Society for Optical Engineering*, *3756*, 277–288.

She, C.-Y., Berger, U., Yan, Z.-A., Yuan, T., Lübken, F.-J., Krueger, D. A., & Hu, X. (2019). Solar response and long-term trend of midlatitude mesopause region temperature based on 28 Years (1990–2017) of Na lidar observations. *Journal of Geophysical Research: Space Physics*, *124*(8), 7140–7156. https://doi.org/10.1029/2019JA026759

She, C.-Y., Latifi, H., Yu, J. R., Alvarez, R. J., II, Bills, R. E., & Gardner, C. S. (1990). Two-frequency lidar technique for mesospheric Na temperature measurements. *Geophysical Research Letters*, *17*(7), 929–932. https://doi.org/10.1029/GL017i007p00929

She, C.-Y., Yan, Z.-A., Gardner, C. S., Krueger, D. A., & Hu, X. (2022). Seasonal variations of temperatures and gravity wave activities in the mesopause region above Ft. Collins, CO (40.6°N, 105.1°W). *Journal of Geophysical Research: Atmospheres*, 2021JD036291.

She, C.-Y., & Yu, J. R. (1994). Simultaneous three-frequency Na lidar measurements of radial wind and temperature in the mesopause region. *Geophysical Research Letters*, *21*(17), 1771–1774. https://doi.org/10.1029/94GL01417

Smith, A. K., Marsh, D. R., Mlynczak, M. G., & Mast, J. C. (2010). Temporal variations of atomic oxygen in the upper atmosphere from SABER. *Journal of Geophysical Research*, *115*(D18), D18309. https://doi.org/10.1029/2009JD013434

States, R. J., & Gardner, C. S. (2000). Thermal structure of the mesopause region (80-105 km) at 40°N Latitude. Part II: Dirunal variations. *Journal of the Atmospheric Sciences*, *57*(1), 78–92. https://doi.org/10.1175/1520-0469(2000)057<0078:TSOTMR>2.0.CO;2

Strelnikova, I., Baumgarten, G., & Lübken, F.-J. (2020). Advanced hodograph-based analysis technique to derive gravity-wave parameters from lidar observations. *Atmospheric Measurement Techniques*, *13*(2), 479–499. https://doi.org/10.5194/amt-13-479-2020

Swenson, G. R., Salinas, C. C. J. H., Vargas, F., Zhu, Y., Kaufmann, M., Jones, M., et al. (2019). Determination of global mean eddy diffusive transport in the mesosphere and lower thermosphere from atomic oxygen and carbon dioxide climatologies. *Journal of Geophysical Research: Atmospheres*, *124*(23), 13519–13533. https://doi.org/10.1029/2019JD031329

Swenson, G. R., Vargas, F. A., Jones, M., Jr, Zhu, Y., Kaufmann, M., Yee, J. H., & Mlynczak, M. (2021). Intra-annual variation of eddy diffusion (k_{zz}) in the MLT from SABER and SCIAMACHY atomic oxygen climatologies. *Journal of Geophysical Research: Atmospheres*, *126*(23), e2021JD035343. https://doi.org/10.1029/2021JD035343

Swenson, G. R., Yee, Y., Vargas, F. A., & Liu, A. Z. (2018). Vertical diffusion transport of atomic oxygen in the mesopause region consistent with chemical losses and continuity: Global mean and interannual variability. *Journal of Atmospheric and Solar-Terrestrial Physics*, *178*, 47–57. https://doi.org/10.1016/j.jastp.2018.05.014

Vadas, S. L., & Becker, E. (2019). Numerical modeling of the generation of tertiary gravity waves in the mesosphere and thermosphere during strong mountain wave events over the Southern Andes. *Journal of Geophysical Research: Space Physics*, *124*(9), 7687–7718. https://doi.org/10.1029/2019JA026694

Walterscheid, R. L. (1981). Dynamical cooling induced by dissipating internal gravity waves. *Geophysical Research Letters*, *8*(12), 1235–1238. https://doi.org/10.1029/GL008i012p01235

Walterscheid, R. L., & Hickey, M. P. (2009). Gravity wave ducting in the upper mesosphere and lower thermosphere duct system. *Journal of Geophysical Research*, *114*(D19), D19109. https://doi.org/10.1029/2008JD011269

Walterscheid, R. L., & Hocking, W. K. (1991). Stokes diffusion by atmospheric internal gravity waves. *Journal of the Atmospheric Sciences*, *48*(20), 2213–2230. https://doi.org/10.1175/1520-0469(1991)048<2213:SDBAIG>2.0.CO;2

Walterscheid, R. L., & Schubert, G. (1989). Gravity wave fluxes of O_3 and OH at the nightside mesopause. *Geophysical Research Letters*, *16*(7), 719–722. https://doi.org/10.1029/GL016i007p00719

Wang, L., Geller, M. A., & Alexander, M. J. (2005). Spatial and temporal variations of gravity wave parameters, Part I: Intrinsic frequency, wavelength, and vertical propagation direction. *Journal of the Atmospheric Sciences*, *62*(1), 125–142. https://doi.org/10.1175/JAS-3364.1

Weinstock, J. (1983). Heat flux induced by gravity waves. *Geophysical Research Letters*, *10*(2), 165–167. https://doi.org/10.1029/GL010i002p00165

Yu, Y., & Hickey, M. P. (2007). Numerical modeling of a gravity wave packet ducted by the thermal structure of the atmosphere. *Journal of Geophysical Research*, *112*(A6), A06308. https://doi.org/10.1029/2006JA012092